UNIVERSITÉ
CAEN
NORMANDIE

Scintillation-Based Dosimetry: Assessing Alpha-Particle and X-Ray Radiations in *In-Vitro* Conditions

EMJMD in Nuclear Physics

Ania Tato Iglesias

Gaston Emanuel Cisterna

Tutor and Co-Tutor:

Anne-Marie Frelin and Saba Ansari-Chauveau

January, 2024

Contents

Chapter 1

Introduction

In the area of Targeted Radiotherapy (TRT), in which a radiopharmaceutical is injected to the patient to selectively target and destroy cancer cells while sparring surrounding tissues, Targeted Alpha Therapy (TAT) has emerged as a promising approach, particularly for the treatment of small, disseminated metastases and lesions situated in sensitive environments [1]. The distinctive characteristics of α-particles, their short range in biological tissue and high linear energy transfer (LET) allow for precise and targeted delivery of radiation, concentrating the destructive effects to the immediate vicinity of cancer cells. Thus α-particles can generate higher damage to the cancer cells than low LET radiation, due to their ability to produce more double strand breaks (DSB) in the DNA [2, 3].

Central to the success of TAT is the development of sophisticated targeting agents to which the α-emitting isotope can be linked to form a radiopharmaceutical. These agents, antibodies, peptides, or other molecules, are designed to specifically recognize and bind to proteins or receptors that are overexpressed on cancer cells or their close environment. This approach allows to deliver α-particles with pinpoint accuracy to the cancer cells, optimizing therapeutic efficacy while minimizing off-target effects [1].

As the development of new radiopharmaceuticals continues to evolve, the evaluation of their therapeutic efficacy becomes paramount. In traditional *in-vitro* assays, the injected activity is a standard factor for assessing radiobiological effects such as cell survival or DSB rate, which are

related to the dose delivered to the cells. In TRT, this quantity is given by the Medical Internal Radiation Dose (MIRD) formalism [4], which correlates absorbed dose with the injected activity through a global S-factor related to the fraction of energy deposited in the target. However, it has to be taken into account that the spatial distribution of radionuclides within the *in-vitro* culture significantly impacts the dosimetric calculations, as shown in previous studies [5]. The indetermination of this distribution can lead to significant errors in the measured dose.

Experiments regarding the high-resolution detection of α-particles' tracks in scintillators have already been carried out [6]. Studies have shown that it is possible to obtain images of the tracks performed by the α-particles (see Figure 1.0.1 for an example) that could help determine the initial distribution of the radionuclides in *in-vitro* configurations.

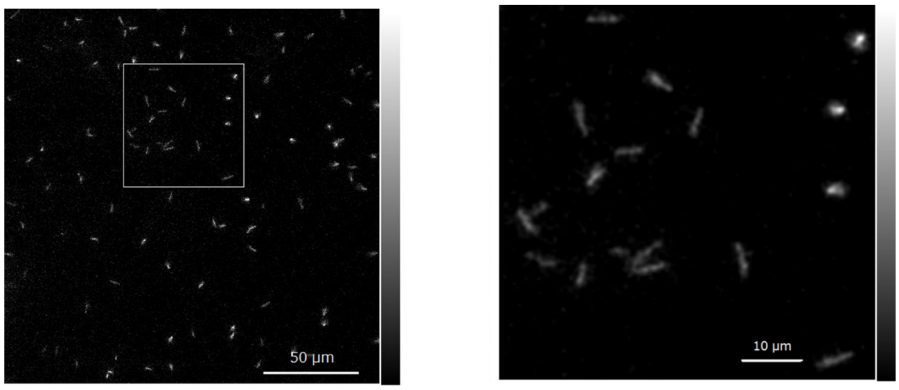

(a) (b)

Figure 1.0.1: a) Image of low energy α-particles in scintillator plate and b) magnified image of area in square (from [6]).

This study focuses on determining the ability of scintillator detectors to provide 2D measurements of energy and dose deposition by α-particle sources in *in-vitro* configurations with a sufficient spatial resolution to detect α-particle interactions and dose deposition at the scale of cells (around 20 μm). This could be useful to determine the spatial distribution of the α-particle emissions and correlate more accurately the absorbed dose in cells with the biological effect of the radiation.

It is also interesting to compare the biological effects of TAT with other radiotherapy treatments like X-ray external beam radiotherapy (EBRT) [5, 7]. In this report, the possibility of employing

the same experimental setup for α-particle dosimetry and X-ray dosimetry in *in-vitro* conditions is investigated. In particular, the possibility to detect scintillation light for the doses deposited by the X-rays is explored.

The characteristics and performance of two scintillators in the evaluation of the magnitudes mentioned above for both α-particle and X-ray irradiation are evaluated through Monte Carlo (MC) simulations using GATE [8]. Two different simulations methods are tested and their characteristics regarding computation time and accuracy of results are addressed.

Chapter 2

Materials and methods

In this chapter, the geometry of *in-vitro* irradiations is described and an introduction to the simulation program is given.

2.1 *In-vitro* dosimetry configuration

2.1.1 α-particle irradiation

The goal of *in-vitro* assays in TAT is to assess the biological effect of α-particle irradiation on the cells (for example, the cell survival) as a function of the delivered dose to the cells. In *in-vitro* assays, cells are located at the bottom of a culture well with α-particle emitting radio-isotopes diluted in the culture medium. Then, when the radio-isotope is attached to the target protein or enzyme on the surface of the cells as shown in Figure 2.1.1 a), the origin of the α-particle emission can be traced to the cells. If a thin bottom culture well is used, a detector can be placed under the well to record the energy of α-particles emitted (see Figure 2.1.1 b)) which will depend on their path along the culture medium.

2.1.2 X-ray irradiation

Another way of performing *in-vitro* irradiation of tumor cells is to use an external beam. When using X-rays to perform the irradiation of the culture medium the external beam comes from an

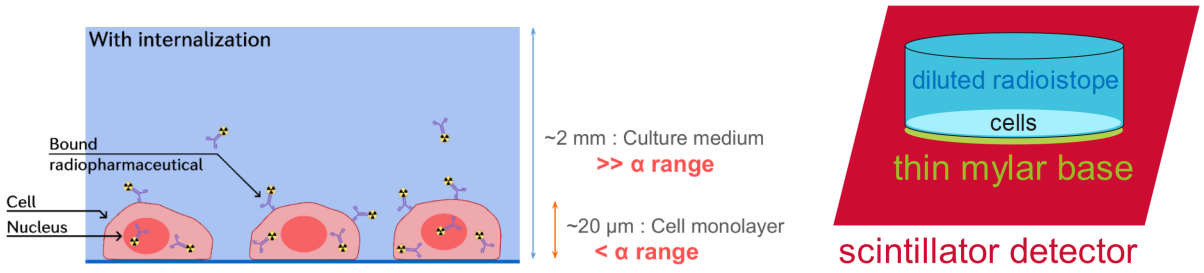

(a) (b)

Figure 2.1.1: a) Culture well and b) experimental configuration for *in-vitro* α-particle dosimetry

X-ray tube. A miniature X-ray tube can be used as it allows to perform live-cell microscopy if mounted on the stage of a microscope with a camera as shown in Figure 2.1.2. With this configuration, the detector can be placed below the sample, in the same way as with the α-particle irradiation.

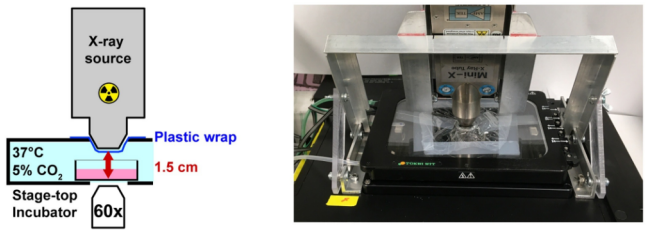

Figure 2.1.2: A scheme and photograph of a miniature X-ray tube on the stage of an inverted microscope are provided. Cells are kept in an incubator for constant temperature and humidity. The nozzle of the miniature X-ray tube is inserted into a circular whole in the incubator lid and a layer of plastic wrap prevents loss of humidity [7].

2.2 Tested scintillators

Two scintillators were studied for both α-particle and X-ray irradiations. The first one was the EJ-212 PMMA plastic scintillator from Ejen Technology and the second one was a $Gd_3Al_2Ga_3O_{12}$ (GAGG) scintillator detector. Their properties are collected in Table 2.2.1.

It must be noted that in a real experiment a specific camera setup with appropriate optical properties to detect scintillation light is employed. In this work, such a system is not taken into

account.

Name	Density [g/cm^3]	Light emission (10^4 ph/MeV)	Thickness (mm)
GAGG	6.630	4.5-5.0	0.05
EJ-212	1.023	1.0	2.00

Table 2.2.1: Characteristics of the scintillation materials used for the simulation.

2.3 MC simulations

The simulations performed in this study aim to reproduce the geometries specified above for dose and energy deposition measurements. The performance of the scintillators was studied for both configurations (α-particle and X-ray irradiation) via MC simulations.

The MC simulations were performed using Gate (Geant4 Application for Tomographic Emission) which is an advanced open software based on the Geant4 toolkit and dedicated to numerical simulations of medical imaging and radiotherapy.

2.3.1 Geometrical configurations

α-particle irradiation

In this study, the configuration presented in Figure 2.1.1 was modelized by a simple geometry shown in Figure 2.3.1 a), containing a scintillator detector voxelized with voxels of 1 μm x 1 μm x 5 mm as shown in Figure 2.3.1 b) (this voxelization is representative of a high spatial resolution for the recording the scintillation with a camera) with a 0.02 mm water layer on top to account for the cells at the bottom of the culture well. The α-emitting isotope diluted in the culture medium was also simplified and modeled as a single point source placed in vacuum above the water layer.

In a second configuration, the point source was placed directly in contact with the scintillator to characterize the intrinsic response of the detector to α-particle irradiation.

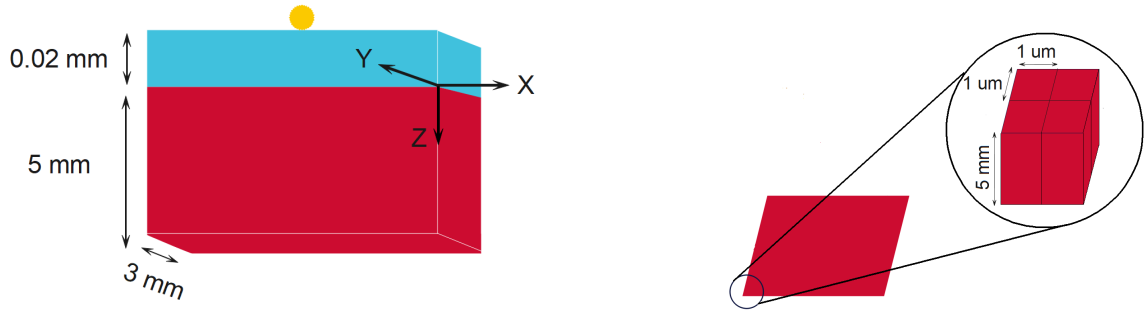

(a) (b)

Figure 2.3.1: a) Configuration for the *in-vitro* experiment simulation with scintillator in red, water layer in blue and source in yellow. b) Schematization of the detector's voxelization.

In both cases, two different definitions of the α-particle emission were implemented and coupled to different simulation tools (see 2.3.2). The first source definition (noted as *Source 1* in the following) shown in Figure 2.3.2 a) represents α-particles emitted from the point source at only one angle φ and θ angles randomly distributed between $\theta = 0°$ and $\theta = 90°$. In the second definition (noted as *Source 2* in the following), α-particles were emitted isotropically with θ between $0°$ and $90°$.

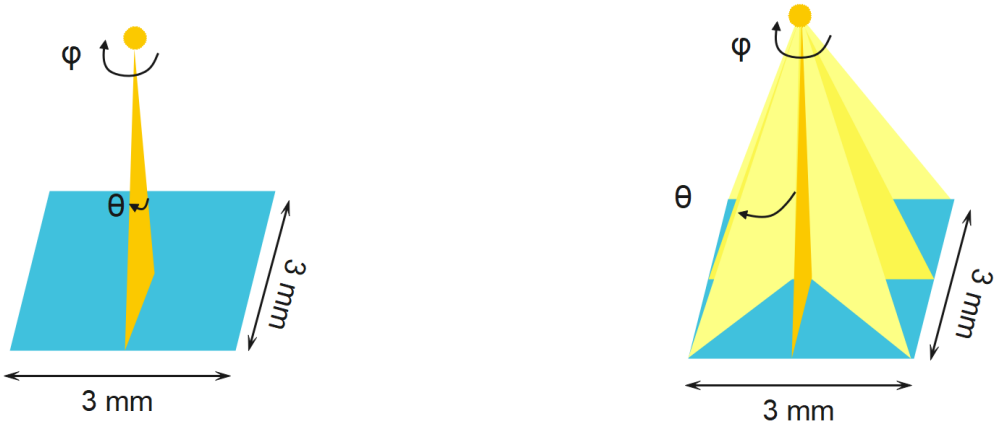

(a) (b)

Figure 2.3.2: a) Source 1: particle beam at $\varphi = 0°$ and θ randomly distributed between $0°$ (perpendicular to the scintillator's plane) to $90°$ (parallel to the scintillator's plane). b) Source 2: isotropic beam between $\theta = 0°$ and $\theta = 90°$. In both cases, the source is placed on top of the water layer, but for better visualization of the irradiation it appears at a certain distance from it.

In all cases, the energy of the α-particles was set to 10 MeV. This energy is of the order of typical energies of α-particles emitted by common radio-isotopes used in TAT, such as ^{212}Pb that subsequently decays to ^{212}Bi, which is an α-particle emitter [5].

X-ray irradiation

In this case, the irradiation configuration presented in Figure 2.1.2 was modelized with a simplified geometry consisting of a plane circular source in air located at 15 mm from the water layer and a scintillator detector directly underneath the water layer (see Figure 2.3.3).

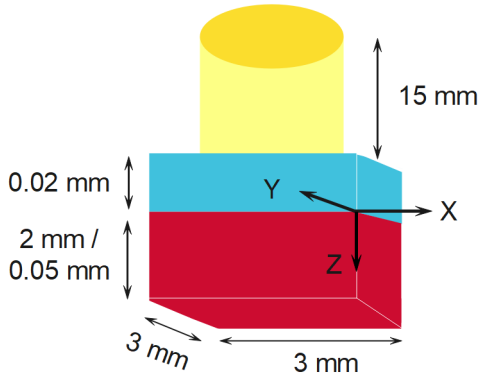

Figure 2.3.3: Geometric configuration for the X-ray irradiation. The thickness of the detector changes according to the detector simulated: 2 mm for the EJ-212 and 0.05 mm for the GAGG.

The simulated X-ray tube was a Mini X2 X-ray tube from Amptek. The energy spectra of the simulated X-rays was provided by the manufacturer and it is illustrated in Figure 2.3.4. The characteristics of the X-ray tube are summarized in Table 2.3.1.

Maximum voltage [kVp]	Tube current [μA]	Target thickness [μm]	Target material	Particle emission rate [ph/s]
50	80	0.75	Silver (Ag)	10^9

Table 2.3.1: Characteristics of the simulated X-ray tube.

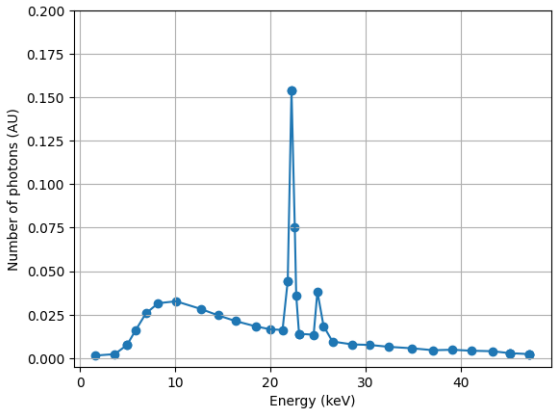

Figure 2.3.4: X-ray spectrum emitted by the Ametek Mini X2 X-ray tube with a silver target.

2.3.2 Simulation characteristics

For both α-particle and X-ray irradiations 10^6 particles were simulated. Secondary particles were not recorded in any of the cases.

Simulations in GATE are divided in a series of steps, such as definition of the simulation environment, definition of the volumes taking place in the simulation, definition of the source and specification of the tools used to interact with the simulation. Regarding the latter, two methods were used: Actors and Systems.

Actors

Actors in Gate gather information such as the energy deposited by particles in a given volume. The actor is attached to the volume of interest, the scintillator in this work. In these simulations, two different actors were used: a PhaseSpace Actor and a Dose Actor

The PhaseSpace Actor was only used for simulations of α-particle irradiation with the *Source 1* configuration. This actor records the characteristics of particles entering the volume to which it is attached, here the scintillator. Its usual function is to split or separate particle tracking, so the phase space of the particles at a certain step of the simulations are saved in a file that is then used as the input file for the ulterior simulation in the detector. This way, the particle emission only has to be simulated once and the whole simulation is speed up if the detection stage of the simulation must be performed several times. In this report, an alternative utility

of the PhaseSpace Actor was studied. It was set to measure the position and the energy of the particle when it enters the volume of the scintillator, the impact direction and the distance covered before it stops (the track length), with the aim of characterizing the energy deposition and the α-particle tracks in the detector.

The Dose Actor was used for both α-particle irradiation with *Source 1* configuration and X-ray irradiation. It stores the dose and the energy delivered to the attached volume (the scintillator) in a 3-dimensional grid that can be personalized to the desired resolution. In this work, the scintillator's surface was divided in 3000 $\times$ 3000 pixels (we use the word *pixel* instead of *voxel* because there is no discretization along the scintillator's thickness) of 1μm $\times$ 1μm for both α-particle and X-ray irradiation, as shown in Figures 2.3.1 and 2.3.3.

Systems

Systems were only used for α-particle irradiation with *Source 2* configuration. Systems provide specific information about the particles' interaction inside the volume of interest, so most of the simulations were performed with them. The PhaseSpace Actor and Systems performances were only compared for the most relevant results, such as the mean behaviour of the particles with respect to the incidence angle θ.

Systems provide a template of a predefined geometry to simulate a sensitive volume. Systems enable the modeling of intricate sensitive volumes, such as scanners, PET scanners, CT scanners, CPET, cylindrical PET, and more. Moreover, systems provide the capability to voxelize the modeled volume. This voxelization is particularly valuable when modeling scintillators and cameras, as described earlier. The most basic system provided by the Systems method is called *scanner*. By creating a scanner, one can discretize the surface of the scintillator into a 2D pixel map. This discrete representation enables the determination of two essential aspects for each alpha particle: discerning the particle's trajectory through the identification of the crossed pixels hit along the particle track and quantifying the energy deposited in each pixel. These two aspects are crucial for the development of the results that will be presented in this study.

2.3.3 Studied parameters

The objective of *in-vitro* dosimetry is to get the energy deposited in the cells, just above the scintillator. For that purpouse, when irradiating the cell sample with α-particles two quantities are relevant: the energy deposited in the detector and the trajectory of the particle in the scintillator. The second one is particularly interesting as it provides information on the particle's track in the cell culture. In this work, the dependence of these quantities on the incidence angle on the scintillator are analyzed, with the aim of reconstructing the emission point of the α-particles.

In the case of the X-rays, only the energy deposited in the detector is of interest. Herein, the deposited energy and dose rates by the X-rays on the scintillator are calculated, and the possibility of detecting the scintillation photons with a camera is explored.

Chapter 3

Results

3.1 α-particle irradiation

3.1.1 Trajectories

α-particles' trajectories across the water layer and the scintillator were considered straight, due to their high mass and LET. The PhaseSpace Actor does not record the interactions of α-particles inside the scintillator, in contrast to Systems, which do provide the interaction points of the particles with each pixel. To confirm the accuracy of the straight-line trajectory assumption, the simulation was performed using Systems.

The simulation was performed with the EJ-212 scintillator and the water layer in place. Nine particles were randomly chosen from the 10^6 simulated particles and their trajectories given by positions where they interact with the scintillator medium were plotted in Figure 3.1.2. It is shown in this Figure that the assumption of the trajectories being straight lines can be applied. Similar results were obtained without the water layer between the source and the scintillator.

To analyze the trajectory of the α-particle, it is important to know not only the shape of the α-particle track, but also their incoming direction. With this objective, the energy deposition of the nine randomly selected particles along with their track was analyzed. The results are shown in Figure 3.1.2 and 3.1.3. It is observed that a greater amount of energy is deposited in the

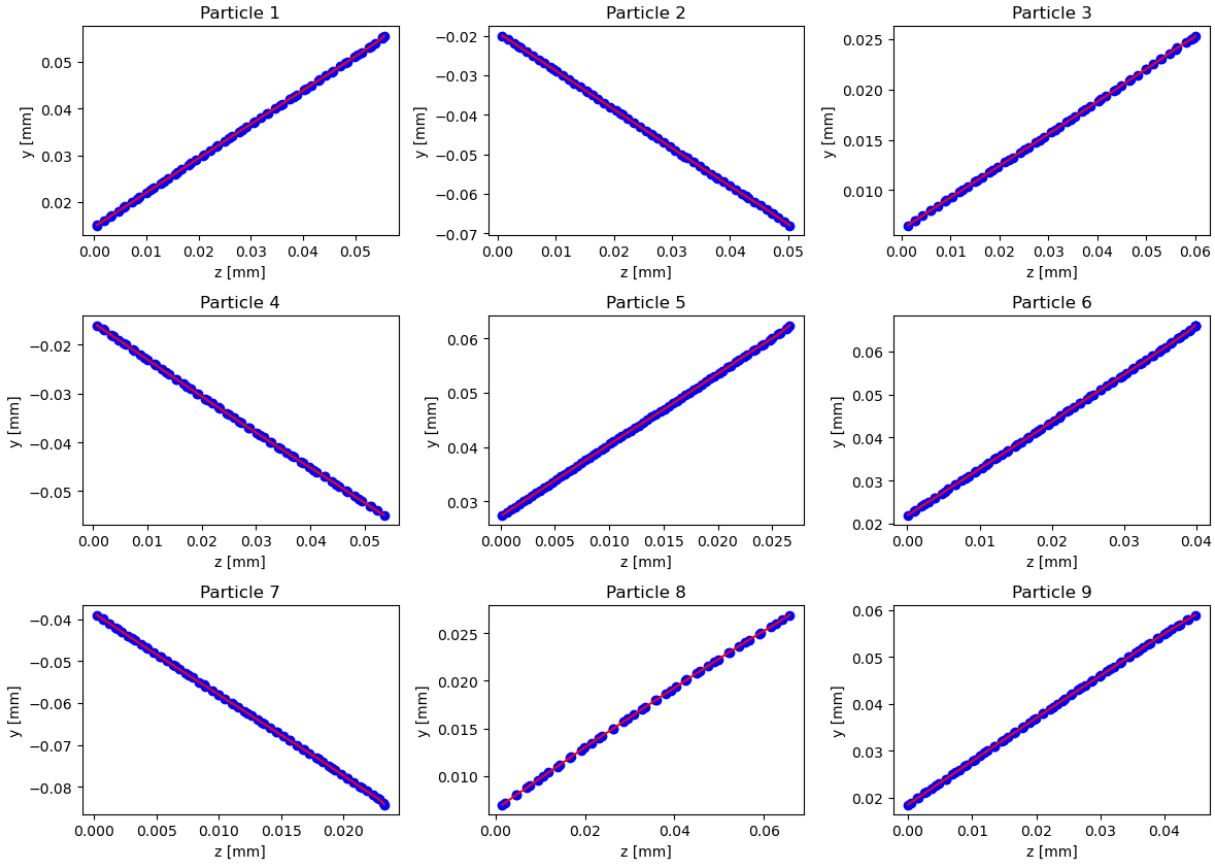

Figure 3.1.1: Trajectories of the 9 alpha particles chosen randomly in the Z-Y plane in the EJ-212 scintillator with 20 μm water layer between the source and the detector.

final segments of the track compared to the initial ones due to the bragg peak profile of energy deposition of α-particles. This observation allows to determine the direction of the tracks as the highest energy is deposited at the end of the particle track.

3.1.2 Distribution of the number of pixels crossed by α-particles as a function of the incidence angle θ

In a real-world detector, the track lengths of the particles cannot be directly measured. Instead, the number of pixels crossed by the particles are accounted for. The number of pixels crossed by the α-particle depends on the incidence angle, as a larger incidence angle relative to the detector's plane implies a larger distance crossed in water and thus a higher energy loss across the track before reaching the detector. The relation between the incidence angle and the number

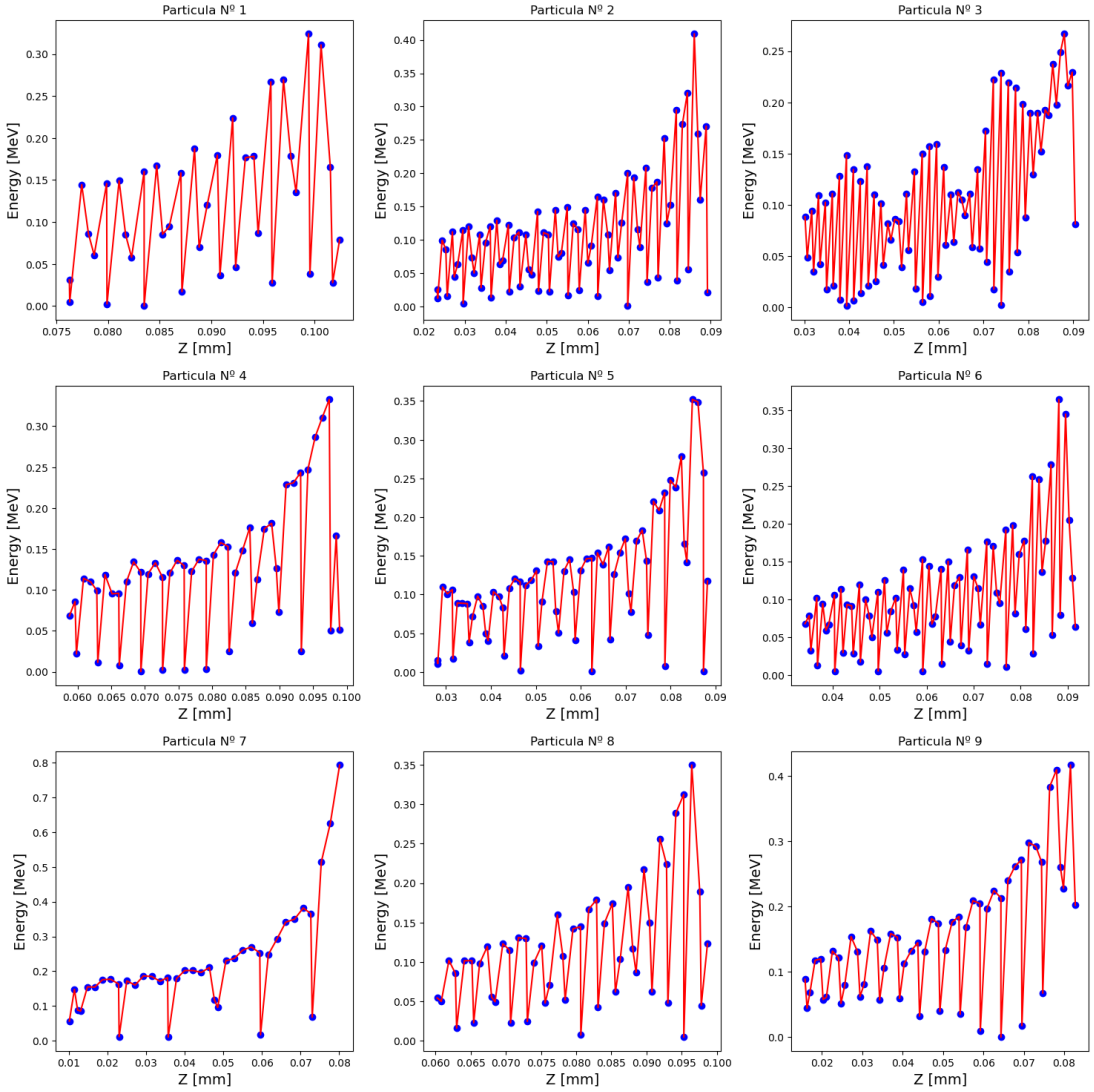

Figure 3.1.2: Trajectories of the nine alpha particles chosen randomly in the Z-Y plane in the detector with a 20 μm water layer between the source and the detector.

of pixels crossed can provide knowledge about the distance traversed and the trajectory of the particle across the water layer that represents the cell culture. This is important in the context of determining the trajectories and the origin of the α-particles in real *in-vitro* experiments with a distribution of radioisotopes in all the culture medium.

Source 2 configuration (see Figure 2.3.2) was used and the simulations were performed using Systems. The number of pixels crossed by the α-particles for different intervals of the incidence angle θ were analyzed. The results are shown in Figure 3.1.4 for both scintillators with and

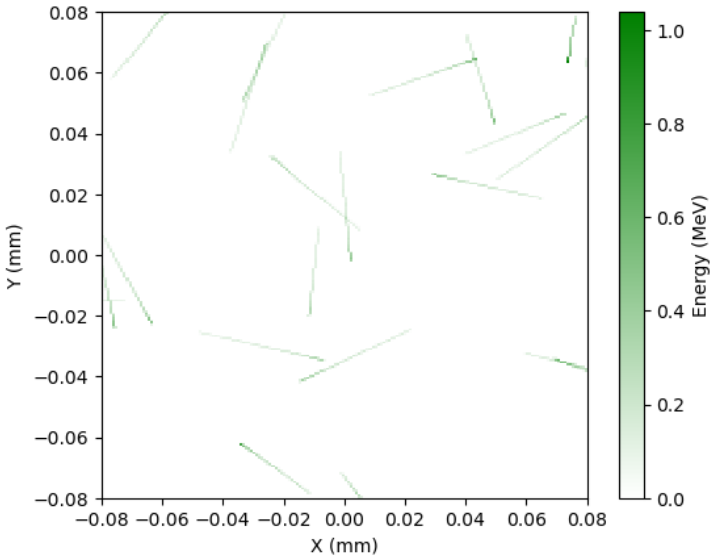

Figure 3.1.3: Energy deposition of α-particles along their tracks. It can be seen that at the end of their trajectories, the energy deposited is higher.

without the water layer between the source and the scintillator.

When comparing the results without the water layer for both detectors, it can be seen that the number of crossed pixels distribution shifts to higher values as the incidence angle increases. This is only due to the scintillator's voxelization.

It can also be observed that GAGG scintillator distributions have a lower mean value than EJ-212 scintillator distributions. This is mainly due to the fact that the GAGG scintillator is six times denser than the EJ-212 scintillator (6.63 $\frac{g}{cm^3}$ vs. 1.02 $\frac{g}{cm^3}$). Consequently, the particles have a much smaller track length in tqqhe GAGG scintillator and the number of crossed pixels is smaller with water as some energy is lost before reaching the scintillator.

The mean value of each distribution shown in Figure 3.1.4 is represented in Figure 3.1.5 for the mean incidence angle. With the water layer, several phenomena appear. It can be seen that above $\theta = 50°$, a substantial increase in the incident angle causes both EJ-212 and GAGG distributions to come back to lower values of crossed pixels. This is because when particles have to travel through the water layer to reach the scintillator, they lose energy. As the angle of incidence increases, so does the track of the particles in water, thus losing more energy and eventually crossing fewer pixels. This behaviour was not seen for distributions without the water layer

where the mean number of pixels crossed increases as the incidence angle increases.

Since particles which travel at $\theta = 90°$ will never reach the detector, there is a greater uncertainty in this final interval (between 85° and 90°), which is why this point was omitted in the Figures.

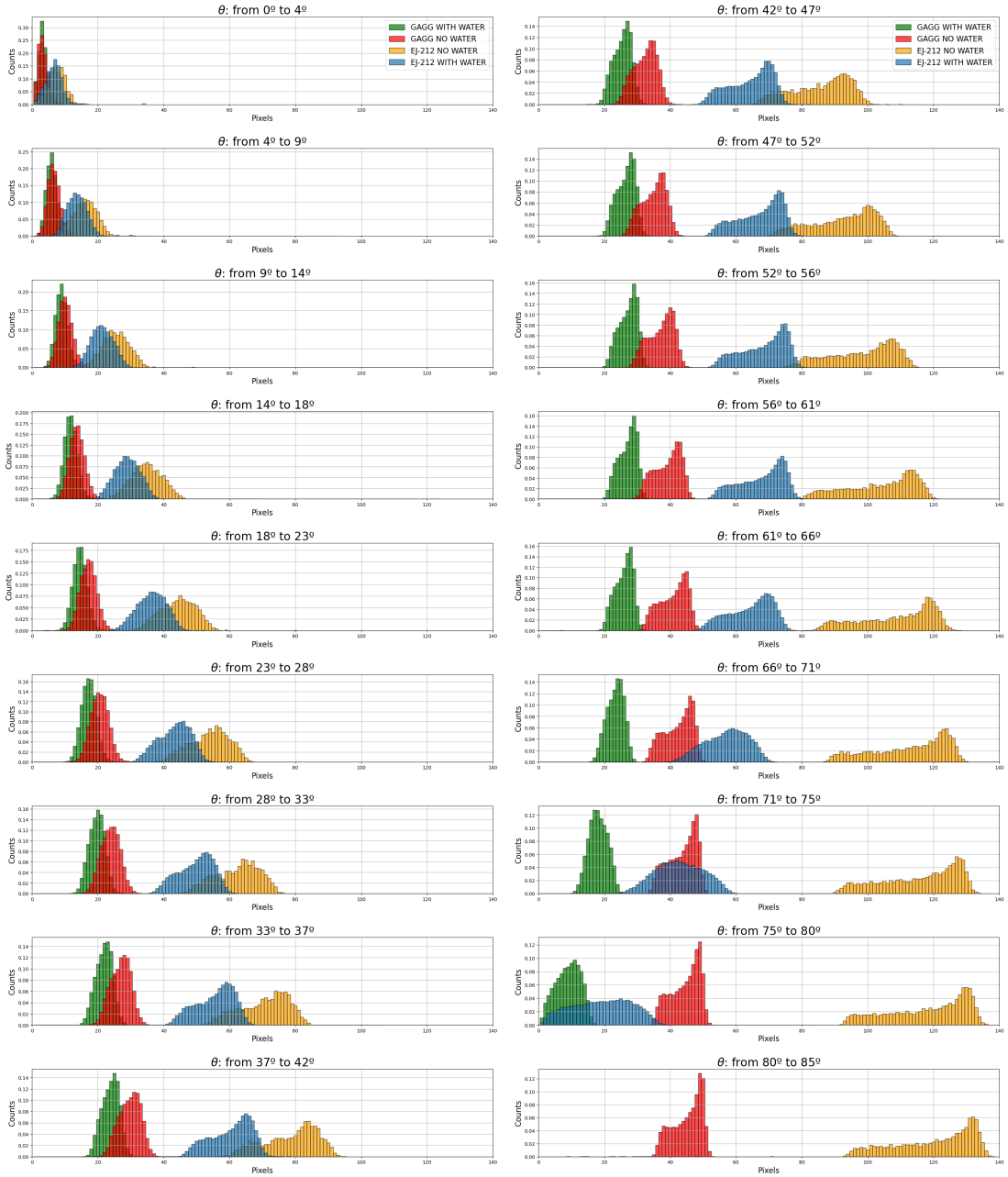

Figure 3.1.4: Number of pixels crossed by α-particles for different intervals of angles θ, for EJ-212 and GAGG detector and with and without water layer.

Finally, the mean number of crossed pixels for the EJ-212 detector were determined using the

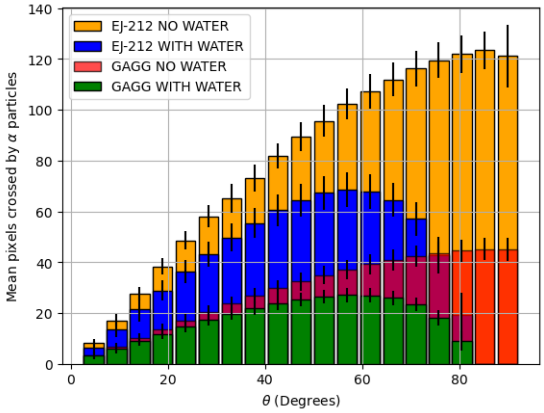

Figure 3.1.5: Mean value of the number of pixels crossed by α-particles for different incidence angles θ using systems for both detectors with and without the water layer.

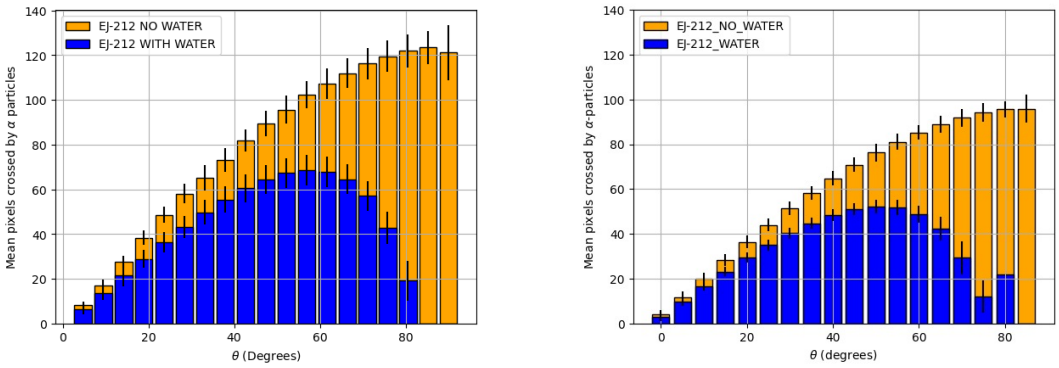

(a) (b)

Figure 3.1.6: Mean value of the number of pixels crossed by α-particles for different incidence angles θ using a) Systems method and b) PhaseSpace Actor for the EJ-212 scintillator.

PhaseSpace Actor. The PhaseSpace output does not specify the pixel the particle has impacted, unlike the System method, which directly provides information of the number of pixels hit by a particle. However, this actor does provide the track length (the distance traversed by the particle from its emission point to the point where it losses all of its energy) and the direction of the particle, through which the number of crossed pixels were approximated by calculating the projection of the α-particle trajectory along the pixelized scintillator plane with a Python routine. As it can be seen by comparing of Figures 3.1.6 a) and b), the amount of crossed pixels are underestimated in the case of the PhaseSpace Actor by a factor of approximately 1.3, but the shape of the distribution and the phenomena obtained with the Systems method are comparable. If the

simulations for a specific geometry are performed with Systems and with the PhaseSpace Actor once, the correction factor for the distributions provided with the PhaseSpace can be calculated by comparisson of the results provided by the two methods. Then, for future simulations of the same geometry only the PhaseSpace Actor could be used, reducing the simulation time significantly (from days to hours), as the Systems method has the disadvantage of longer simulation times.

3.1.3 Distribution of the number of pixels crossed by α-particles as a function of the azimuthal angle φ

This section focuses on the analysis of the dependence of the number of pixels crossed by α-particles on the azimuthal angle φ. For this case, the data is presented in Figure 3.1.7. It illustrates the mean values of crossed pixels by α-particles at different mean angles φ across the entire range in θ. The mean angle φ is the mean angle of the intervals defined by $\Delta\varphi = 4°$, similarly to what was done in Figure 3.1.5.

A discernible pattern of alternating maxima and minima for both type of detectors, each with the same amplitude, is evident. The maxima occur at angles $\varphi_{max} = 45°$, 135°, 225°, and 315°, while the minima are observed at $\varphi_{min} = 0°$, 90°, 180°, and 270°. These angles correspond to instances where particles cross the pixels diagonally and perpendicularly, respectively, as illustrated in Figure 3.1.8. Segments in red represent the particles' trajectories. Both segments have the same length, but when the angle of the segment is 45 degrees for instance (in green), the number of crossed pixels is larger than at 90 degrees (in blue). This explains the pattern described in Figure 3.1.7 but also contributes to the dispersion on the number of pixels crossed (Figure 3.1.4), especially when there is no discretization in φ.

3.1.4 Dependence of deposited energy on the incidence angle θ

While track-lengths provide information on the incidence direction, energy deposition measurements are necessary to discriminate the origin of the emission. Without water layer, particles always deposit the same energy in the detector, in this case 10 MeV, since there is no intermediate medium in which they can lose energy. When a water layer is added, the energy deposition

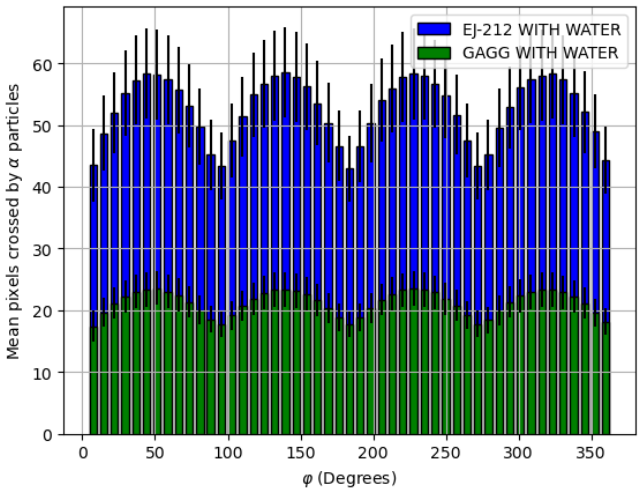

Figure 3.1.7: Mean value of the number of pixels crossed by α-particles for different mean azimuthal angles φ for EJ-212 and GAGG detectors.

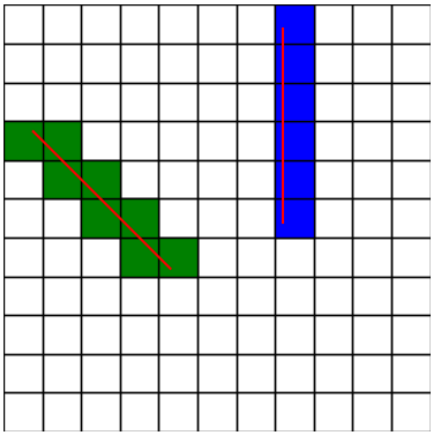

Figure 3.1.8: Visualization depicting variations in the number of crossed pixels for different φ values. The green-colored pixels crossed diagonally represent a track associated with a φ causing a maximum in crossed pixels. Conversely, the blue-colored pixels crossed perpendicularly correspond to a φ resulting in a minimum in crossed pixels. Both segments exhibit tracks (depicted in red) of equal length, corresponding to the same incident angle θ.

depends on the incidence angle due to the different paths of the particles in the water layer. This dependence is shown in Figure 3.1.9, which depicts the mean total energy deposited in the scintillator by α-particles for different mean incidence angles θ, for EJ-212 detector using the PhaseSpace Actor and the Systems method, and for GAGG scintillator using only the Systems

method.

As observed in this case, the PhaseSpace Actor and the Systems method yield the same behaviour, because the PhaseSpace Actor does record the kinetic energy of the particles entering the detector. In this case, the PhaseSpace Actor provides a faster result than the Systems method, so it is a more adequate method to study the dependence of the energy deposited on the incidence angle. Besides, both EJ-212 and GAGG detectors show the same tendency: a decrease when θ increases. This can be explained by the fact that, upon crossing the water layer, particles will deposit the remaining energy in the detector, regardless of whether they cross few or many pixels. At large angles, there is a reduction in the energy deposited in the detectors, attributed to the increased energy deposition in water.

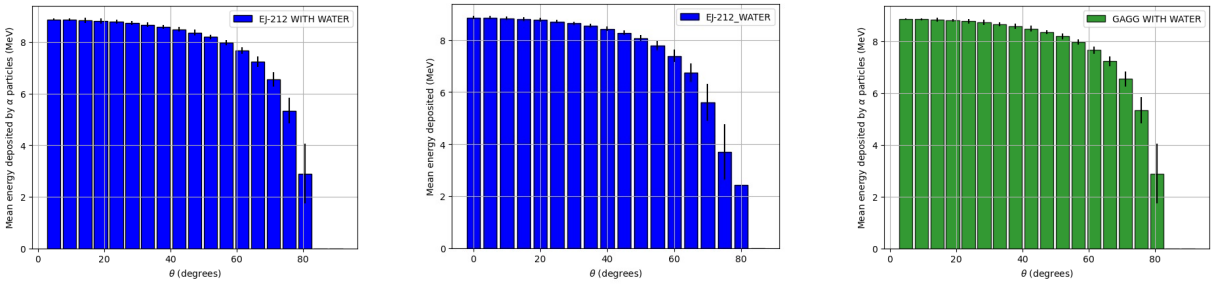

(a) (b) (c)

Figure 3.1.9: Mean energy deposited for different mean incidence angle θ for: a) EJ-212 detector using Systems method, b) EJ-212 detector using PhaseSpace Actor method and c) GAGG detector using Systems method.

3.1.5 Determination of the α-sources' spatial distribution

Understanding radionuclide distribution is crucial in targeted alpha therapy, influencing how alpha particles interact with cells and ensuring precise, uniform doses for effective cancer treatment while minimizing damage to healthy tissues. Utilizing the previous findings (track length and energy distributions), an algorithm was developed to estimate the emission points of α-particles crossing the scintillator, especially in the scenario of having multiple punctual sources.

Approach

The algorithm takes representative inputs of *in-vitro* dosimetric experiments for TAT, such as: the energy deposited per pixel per α-particle, the total energy deposited in the detector per α-particle and the number of pixels crossed by α-particles. These three magnitudes are representative of *in-vitro* dosimetric experiments for TAT and have been studies in this project.

To compute the emission point of α-particles, knowledge of the angles (φ, θ) for each particle is essential. Subsequently, the trajectories of the particles can be projected across the 0.02 mm of water in the directions specified by (φ, θ). It is important to note that the assumption of straight-line trajectories is upheld.

To compute φ, the initial and final pixels of the track must be identified. As shown in Figure 3.1.2, more energy is deposited in the final pixels than in the initial ones due to the bragg peak profile of energy deposition. This disparity facilitates the identification of the track's direction and, consequently, of φ.

To determine θ, interpolation functions for energy deposition and pixels crossed were derived, as shown in Figure 3.1.10 a) and 3.1.10 b).

In Figure 3.1.10 a), the incident angle for α-particles can be interpolated on the red fitted curve for every mean pixel crossed. However, not every mean pixel value corresponds to a unique angle. For instance, in Figure 3.1.10 a) for a mean pixel value of 30, two possible values of the incident angle lie on the red curve: $\theta = 20°$ and $\theta = 79°$.

To select the correct angle, information on the deposited energy from Figure 3.1.10 b) is utilized. The total energy deposited by the particle in the EJ-212 scintillator is 3.69 MeV, as an example. According to the red fit in Figure 3.1.10 b), this energy corresponds to an angle of 79°, one of the interpolated angles from Figure 3.1.9 a). Therefore, utilizing both sources of information, 79° is chosen as the correct angle of incidence. In the case of a slight discrepancy between the angles estimated by these two figures, an average of the two values is taken.

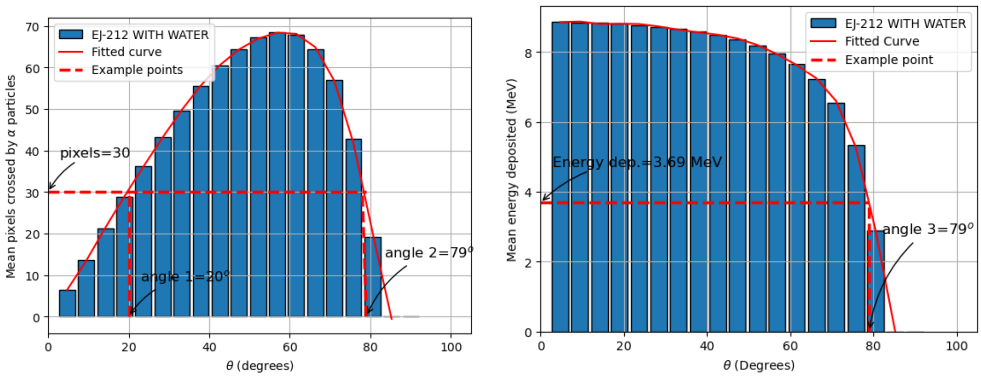

(a) (b)

Figure 3.1.10: a) Incidence angle interpolation for mean pixels crossed by α-particles for EJ-212 scintillator with 20 μm layer of water. b) Deposited energy interpolation as function on the incidence angle for EJ-212 scintillator with 20 μm layer of water.

Results

Simulations involving 100-point sources distributed across the X-Y plane were performed. Two simulation scenarios were examined: one with 2000 primary particles simulated and another one with 10000 primary particles. The energy deposited per pixel for the 2000 particles is depicted in Figure 3.1.11. With this available data, the spatial distribution of the sources is estimated.

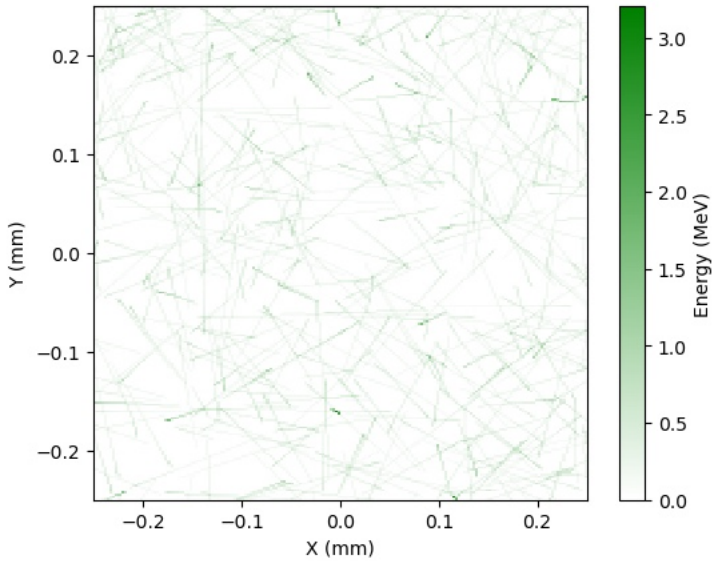

Figure 3.1.11: Energy deposited per pixel for 2000 particles.

The direction (φ, θ) of each particle was determined by the algorithm. Finally, with the knowledge of (φ, θ), the calculated emission points were computed and are presented in Figure 3.1.12.

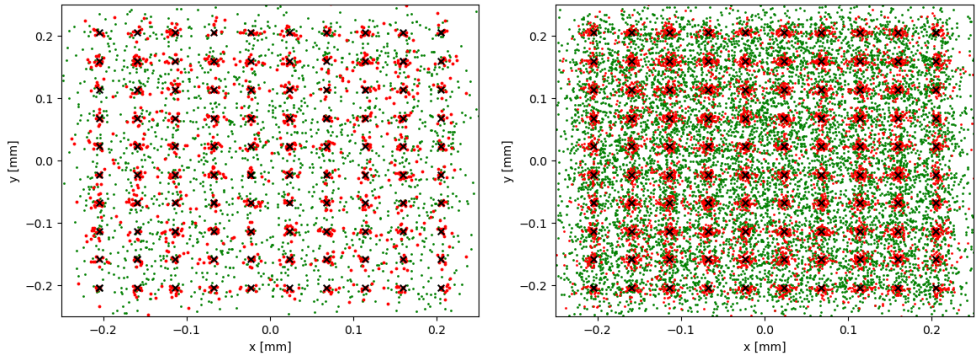

(a) (b)

Figure 3.1.12: Positions of the first pixel hit by α particles in green, real position of the sources in black and position of the sources calculated in red for a) 2000 primary particles and b) 10000 primary particles.

Figures 3.1.13 a) and 3.1.13 b) depict the distribution of absolute errors obtained during the calculation of (φ,θ) using the algorithm described. Notably, in the variable θ the observed error is more pronounced than in φ. If it's considered the maximum error in θ observed in Figure 3.1.13 (a) as $|\theta_{sim} - \theta_{cal}|_{max} \approx 15^o$, the error in the position of the source, once projected across the 20 μm distance, is approximately less than 6 μm.

It should be noted that this algorithm is basic and serves as motivation for the utilization of the results obtained in this study. The algorithm does not account for the spatial distribution of sources varying along the z-direction. In other words, each point source may have a different water thickness between itself and the scintillator and the algorithm does not take this into account. It also does not consider the possibility that sources may not be point-like. In all such cases, this algorithm is incapable of reproducing accurate results. Nevertheless, it serves as a promising starting point for future developments.

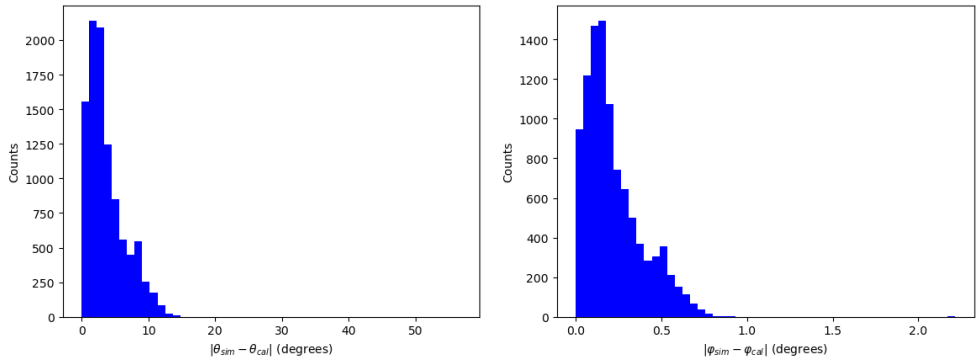

(a) (b)

Figure 3.1.13: a) Absolute error distribution between θ_{sim} (simulated) and θ_{cal} (calculated) with 10000 primary particles simulated. b) Absolute error distribution between φ_{sim} (simulated) and φ_{cal} (calculated) with 10000 primary particles simulated.

3.2 X-ray irradiation

The X-ray irradiation configuration differs from the α-particle irradiation configuration because, contrary to α-particle irradiation where few particles are able to deposit high amounts of energy, in X-ray irradiation many photons deposit a small amount of energy. Consequently, the dosimetric method must be adapted.

The geometry depicted in Figure 2.3.3 was simulated for the whole X-ray fluence and for the two scintillator detectors. The Dose Actor was used, due to its lower simulation time. The deposited dose rate was obtained, and it is shown in Figure 3.2.1. As it can be seen, the dose deposited in the GAGG scintillator is much higher due to its higher density.

The energy rate and the dose rate deposited in the beam area and the rate of scintillated photons were calculated. The results are collected in Table 3.2.1.

As it can be observed, there is a large difference between the dose delivered in the GAGG scintillator in comparisson with the EJ-212 scintillator. This is due to two reasons: the density and the thickness of the detectors. The thickness of the GAGG scintillator is 0.05 mm whereas for the EJ-212 scintillator the thickness is of 2 mm, so there is a difference of two orders of magntide in the thickness, or equivalently in the volume. In the density, there is a factor six

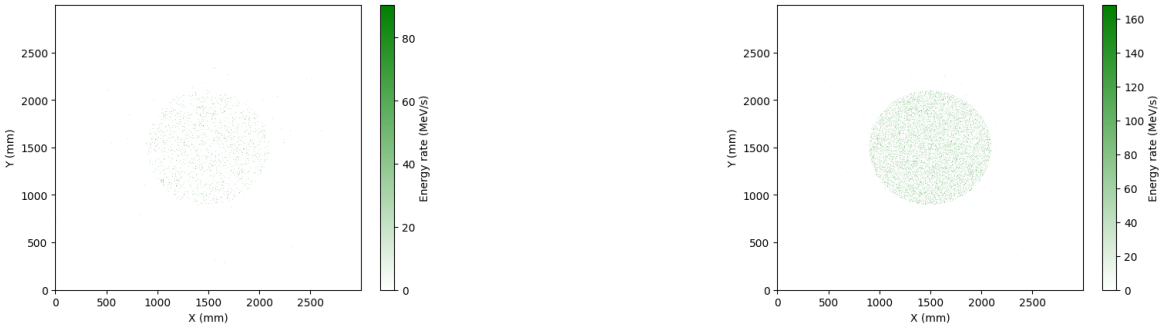

(a) (b)

Figure 3.2.1: 2D plot of the dose rate produced by the X-rays in the scintillator detector for 10^6 simulated particles for the a) EJ-212 scintillator and b) the GAGG scintillator.

Detector	Scintillation photon rate (ph/s)	Energy rate (MeV/s)	Dose rate (Gy/s)
EJ-212	1.44×10^{10}	1.44×10^{6}	3.59×10^{-4}
GAGG	5.46×10^{11}	1.15×10^{7}	1.77×10^{-2}

Table 3.2.1: Scintillation photon rate, energy rate and dose rate deposited in the detector.

difference btween the EJ-212 and the GAGG, which causes an order of magnitude difference in the energy, along with the fact that the GAGG photoelectric attenuation is two orders of magnitude higher than in the EJ-212. It is known that the dose is the energy per mass unit. Considering the mass as the density times the volume, the two orders of magnitude difference in the deposited doses is explained.

Only the dose rate calculated for the GAGG scintillator seems enough for the detection of scintillation light with a camera, as studies show that the minimum dose measurable with a camera is of 1.15×10^{-2} Gy/s [9]. Thus, GAGG scintillator appears better suited for measurements of the scintillation light due to X-ray irradiation, as it will need a less sensitive camera, which is easier and cheaper to achieve.

Chapter 4

Conclusions

This study focused on assessing the ability of two scintillator detectors (EJ-212 and GAGG scintillators) to provide 2D measurements of energy and dose deposition of α-particles and X-rays in *in-vitro* configurations. The analysis was performed via MC simulations using the software Gate. Two different methods were used to interact with the simulations (PhaseSpace Actor method and Systems method).

In the study of α-particle irradiation, trajectories were considered straight, justified by their high mass and Linear Energy Transfer (LET). Verification using the Systems method confirmed this assumption. Analysis of energy deposition along particle tracks revealed a significant deposition increase in the final segments, allowing the determination of track direction.

The relationship between incidence angles in the scintillator, θ and φ, and the number of pixels crossed by the α-particles was explored. This study revealed that the number of pixels crossed by the α-particles as a function of the polar angle θ shows different behaviours depending on the scintillator material used. The GAGG scintillator, being denser, exhibited narrower distributions (less dispersed with respect to the angle) and lower values of the number of pixels crossed compared to EJ-212. Thus, the GAGG scintillator seems recommended for α-particle dosimetry to cells, as it allows better identification of the incidence angle due to the smaller dispersion already mentioned. Besides, the number of pixels crossed by the α-particles in the GAGG scintillators are smaller and of the order of the cell dimmension, which is important for a good spatial resolu-

tion, as shorter track lengths allow for more precise localization of α particle interactions within the scintillator material. Concerning the φ angle, a distinct pattern of maxima and minima in the distribution of pixels crossed with respect to the azimutal angle φ was observed. This pattern was more pronounced in the EJ-212 distribution due to its lower density, which is also in favour of the GAGG.

The two simulation methods were compared for the most relevant results of the α-particle irradiation. It was found that the PhaseSpace Actor method and the Systems method provide the same behaviour for the pixels crossed by the α-particle with respect to the polar incidence angle θ, but the PhaseSpace Actor method underestimates the number of pixels crossed by the α-particles. Thus, the Systems method is considered to provide a more accurate result of the amount of pixels crossed by the α-particles and should be used if precise calculations are needed. If only the behaviour of the pixels crossed distribution is needed, the PhaseSpace Actor provides a much faster result (from days to hours) and could be used to optimize the computation process.

The energy deposition dependence on incidence angle θ was also investigated. Both EJ-212 and GAGG scintillators showed a reduction in energy deposition at larger angles, above $50°$, due to increased energy loss in water. For these calculations, both Systems method and PhaseSPace Actor method provide the same result.

An algorithm was developed to estimate emission points of α-particles from the energy deposition and number of pixels crossed in the scintillator. Results indicated the feasibility of determining spatial distribution for multiple punctual sources placed at the same distance from the scintillator. Future studies on the posibility of determining the spatial distribution with different distances to the scintillator detector must be performed.

In the case of the X-ray irradiation, it was found that the dose deposited by the X-rays was enough to produce scintillation light to be detected by a camera only in the GAGG scintillator because, as indicated in the literature (see [9]), cameras can detect scintillation light produced by deposited doses above 1.15×10^{-2} Gy/s. It was also shown that the dose deposited in the GAGG scintillator was much higher for the same X-ray energy spectrum, thus the use of GAGG for this kind of assays is recommended.

All these results were obtained for simplified geometries of the real experiments, but they show that it is possible to obtain important information for both α-particle and X-ray dosimetric assays. Simulations of geometries closer to the real experimental set ups are required in the future for comparison with these results. Manageable improvements to the simulations presented in this work could be done by simulating volumetric α-sources instead of point sources or by considering the angular spread of the X-ray beam delivered by the X-ray tube for X-ray irradiation. Finally, more realistic spatial resolution (the size of the voxels for instance) should also be considered.

Bibliography and References

[1] Alexis Doudard, Aurélien Corroyer-Dulmont, Cyril Jaudet, Myriam Bernaudin, Samuel Valable, Xavier Ledoux, and Anne-Marie Frelin-Labalme. Application of a new spectral deconvolution method for in vitro dosimetry in assessment of targeted alpha therapy. *American Association of Physicists in Medicine*, 2022. 1

[2] Stefan J Roobol, Irene van den Bent, Wiggert A van Cappellen, Tsion E. Abraham, Maarten W. Paul, Roland Kanaar, Adriaan B. Houtsmuller, Dik C. van Gent, and Jeroen Essers. Comparison of high- and low-let radiation-induced dna double-strand break processing in living cells. *PubMed Disclaimer*, 2020. 1

[3] Ysabella Kassandra Ong. Detector geometry studies for beta detection in targeted alpha therapy. *PubMed Disclaimer*, 2023. 1

[4] SMO Ramos, S Thomas, MA Pinheiro, ARFB Coelho, M Albernaz, CLG Dos Santos, MBT Berdeguez, F Zikan, PDC Medeiros, DDCP Sampaio, et al. Internal radiation dose and modeling codes in nuclear medicine: A fresh look at old problems. *Int J Radiol Radiat Ther*, 4(5):00111, 2017. 2

[5] Anne-Marie Frelin-Labalme, Thomas Roger, Nadia Falzone, Boon Quan Lee, Nicola R. Sibson, Katherine A. Vallis, Myriam Bernaudin, Samuel Valable, and Aurélien Corroyer-Dulmont. Radionuclide spatial distribution and dose deposition for in vitro assessments of 212pb-vcam-1 targeted alpha therapy. *Medical Physics*, 47(3):1317–1326, 2020. 2, 8

[6] Seiichi Yamamoto, Masao Yoshino, Kei Kamada, Ryuga Yajima, Akira Yoshikawa, Kohei Nakanishi, and Jun Kataoka. Development of an ultrahigh resolution real time alpha particle

imaging system for observing the trajectories of alpha particles in a scintillator. *Scientific reports*, 13(1):4955, 2023. 2

[7] Surendra Prajapati, Maëlle Locatelli, Caleb Sawyer, Julia Holmes, Keith Bonin, Paul Black, and Pierre-Alexandre Vidi. Characterization and implementation of a miniature x-ray system for live cell microscopy. *Mutation Research/Fundamental and Molecular Mechanisms of Mutagenesis*, 824:111772, 2022. 2, 5

[8] OpenGATE collaboration. Gate, 2023. `http://www.opengatecollaboration.org/`. 3

[9] Jonathan Boivin, Sam Beddar, Maxime Guillemette, and Luc Beaulieu. Systematic evaluation of photodetector performance for plastic scintillation dosimetry. *Medical Physics*, 42(11):6211–6220, 2015. 25, 27